Acta Crystallographica Section D
Biological Crystallography
ISSN 0907-4449

Structure of agkistrodotoxin in an orthorhombic crystal form with six molecules per asymmetric unit

Liang Tang,[a] Yuan-Cong Zhou[b] and Zheng-Jiong Lin[a]*

[a]National Laboratory of Biological Macromolecules, Institute of Biophysics, Academia Sinica, Beijing 100101, People's Republic of China, and [b]Shanghai Institute of Biochemistry, Academia Sinica, Shanghai 200031, People's Republic of China

Correspondence e-mail: lin@sun5.ibp.ac.cn

Received 22 July 1998
Accepted 4 October 1999

PDB Reference: agkistrodotoxin, 1bjj.

The structure of agkistrodotoxin crystallized under basic conditions has been determined at 2.8 Å resolution by the molecular-replacement technique and refined to a crystallographic *R* factor of 0.194 and a free *R* factor of 0.260 with good stereochemistry. The molecular packing in the crystal differs from other PLA_2s. The six molecules in the asymmetric unit form three dimers linked by Ca^{2+} ions in a near-perfect six-ligand octahedral coordinating system. Extensive intermolecular hydrophobic interactions occur at the interfacial recognition site of each neurotoxin molecule, which provides an insight into phospholipase A_2–membrane interactions. This hydrophobic interaction-induced molecular association along the interfacial recognition site suggests a self-protection mechanism of agkistrodotoxin.

1. Introduction

Agkistrodotoxin (ATX) is a potent presynaptic neurotoxin purified from the venom of *Agkistrodon halys* Pallas (*A. blomhoffii* Brevicaudus), a Chinese pit viper living in the Jiangsu and Zhejiang provinces (Chen *et al.*, 1981, 1987; Zhang *et al.*, 1981). It functions at the presynaptic level by a typical triphasic modulation of neurotransmitter release, *i.e.* initial depression, subsequent facilitation and final blockade of neurotransmission. The minimum lethal dose is 0.055 mg kg^{-1} in mice. ATX is also a group II secretory phospholipase A_2 (PLA_2) composed of 122 amino-acid residues cross-linked by seven disulfide bonds, with a molecular weight of 13400 Da and an isoelectric point of 6.9 (Chen *et al.*, 1981; Kondo *et al.*, 1989). The PLA_2 activity is essential for ATX to exert its neurotoxicity.

A number of secretory PLA_2 presynaptic neurotoxins have been isolated from snake venoms (for reviews, see Yang, 1994; Hawgood & Bon, 1991; Tzeng, 1993; for reviews on PLA_2, see Arni & Ward, 1996; Mukherjee *et al.*, 1994; Dennis, 1994). Some of them, *e.g.* crotoxin, β-bungarotoxin and vipoxin, are functionally oligomeric proteins consisting of an indispensable PLA_2 subunit and one or more inhibitory or chaperonic subunits, which target the neurotoxins towards the putative acceptors on the presynaptic membrane and/or protect them from non-specific binding. Crotoxin (Bon *et al.*, 1979), a presynaptic neurotoxin from the venom of *Crotalus durissus* Terrificus, is a heterodimer between a basic PLA_2 subunit which is weakly toxic and a chaperonic acidic subunit with neither toxicity nor phospholipase activity. The basic subunit of crotoxin shows an ~81% sequence identity with ATX, while the precursor of the acidic subunit is ~66% identical to the acidic PLA_2 from the same source as ATX. β-Bungarotoxin is a disulfide-bond linked heterodimer composed of a PLA_2 subunit and a Kunitz subunit, which targets the neuro-

Table 1
Data-collection and structure-refinement statistics.

Data collection	
Resolution (Å)	30–2.8
Number of observations	71221
Number of unique reflections	24339
Completeness (outermost shell) (%)	93.9 (92.7)
R_{merge}	0.169
Mosaicity	0.784
Crystallographic refinement	
Resolution (Å)	30–2.8
Number of reflections ($>2\sigma$)	23582
Completeness (outermost shell) (%)	91.2 (88.3)
R	0.194
R_{free}	0.260
Current protein model	5832 atoms, 8 Ca^{2+} ions, 17 water molecules
R.m.s.d. from ideal value	
Bond lengths (Å)	0.007
Bond angles (°)	1.1
Dihedral angles (°)	25.8
Improper angles (°)	0.61
Mean B values (Å^2)	
Protein atoms	33.5
Main-chain atoms	31.6
Side-chain atoms	35.0
Ca^{2+} ions	32.7
Water molecules	35.7
R.m.s.d. for bonded B	4.28

toxin to the potassium channel (Kwong *et al.*, 1995). However, ATX is a single-chain presynaptic neurotoxin with an unusual non-basic isoelectric point of 6.9, which distinguishes ATX from the other strongly basic PLA_2 presynaptic neurotoxins.

ATX has a strong tendency towards self-aggregation, especially at high concentrations, and the state of aggregation varies with the solvent components. Under crystallization conditions, ATX shows crystal-form polymorphism. It has so far been crystallized in at least six crystal forms (Li *et al.*, 1995; Jin *et al.*, 1990; L. Tang and Z.-J. Lin, unpublished results). However, all these crystal forms contain multiple molecules in the asymmetric unit, which causes difficulties in structure determination by the molecular-replacement method (Rossmann & Blow, 1962). The structure of ATX crystallized at pH 4.5 in space group $P2_1$ with eight molecules in the asymmetric unit has been determined (PDB code 1a2a). The structure reveals a 'dimer of dimers'-like molecular aggregation. The molecule contains a surface region with unique conformation and electrostatic characteristics which are remarkably different from those of non-neurotoxic snake-venom PLA_2s. This region might be responsible for the recognition of agkistrodotoxin by the specific acceptor at the presynaptic membrane (Tang *et al.*, 1997, 1998). Studies of the multiple crystal forms of agkistrodotoxin are useful in defining those structural features which might be influenced by the crystal packing and in clarifying whether the aggregation state observed in the $P2_1$ crystal depends on the crystallization conditions. Here, we report the 2.8 Å resolution structure of ATX crystallized at pH 8.5 in space group $P2_12_12_1$ with six molecules per asymmetric unit. The molecular packing shows distinct features. The implications for neurotoxic mechanism and PLA_2–membrane interactions are discussed.

2. Materials and methods

2.1. Protein crystallization and data collection

ATX was purified from the venom of *A. halys* Pallas as previously described (Chen *et al.*, 1981). Crystallization was performed by the sitting-drop vapour-diffusion method (Jin *et al.*, 1990). The droplet was a mixture of 20 µl 10 mg ml^{-1} protein solution and 5 µl 0.6 *M* KCl in 0.1 *M* Tris–HCl buffer pH 8.5 and was equilibrated with 2.0 ml of reservoir solution consisting of 60% MPD (2-methyl-2,4-pentanediol) at 291 K. Crystals appeared within two weeks and belong to the space group $P2_12_12_1$, with unit-cell parameters a = 87.75, b = 105.80, c = 110.03 Å. There may be as many as six molecules in the asymmetric unit according to Matthews statistics (Matthews, 1968); the corresponding V_m value is 3.18 Å^3 Da^{-1}. Data were collected on a MAR imaging-plate detector mounted on a rotating-anode X-ray generator and were processed with the programs *DENZO* and *SCALEPACK* (Otwinowski & Minor, in preparation; Table 1). Diffraction data revealed pseudo-*A*-centring symmetry at low resolution (Jin *et al.*, 1990). A Patterson map calculated at 20.0–5.0 Å resolution showed a spreading non-origin peak near the centre of the crystallographic *A* face with a height of 24% of the origin peak (Fig. 1). The relative height of the non-origin peak to the origin peak was reduced significantly when using higher resolution for the calculation. In a 20.0–3.0 Å Patterson map, the non-origin peak was located at (0, 0.524, 0.484) with a relative height of ∼9%. This indicates that the crystal has pseudo-*A*-centring symmetry and that the pseudo-symmetry breaks down at higher resolution.

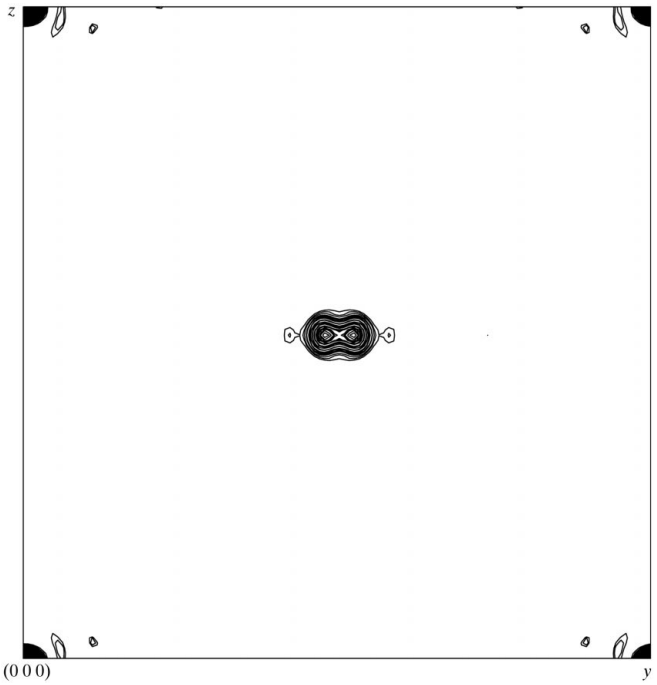

Figure 1
x = 0 section of the Patterson synthesis calculated from the data set in the 20.0–5.0 Å resolution shell. The crystallographic b axis lies along y and the c axis lies along z. y and z vary from 0 to 1. Contouring starts at the 4σ level and the interval is 2σ. A spreading non-origin peak occurs at the centre of the *A* face, indicating the pseudo-*A*-centring symmetry.

2.2. Molecular replacement

Molecular replacement was carried out with the program *AMoRe* (Navaza, 1994) from the *CCP*4 suite (Collaborative Computational Project, Number 4, 1994). One of the eight molecules (chain *A*) of the crystal structure of ATX at pH 4.5 (Tang *et al.*, 1998; PDB entry code 1a2a) was selected as the initial search model and all *B* factors were reset to 20 Å^2. A cross-rotation function was calculated with 12–3.5 Å resolution data and an integration radius of 20 Å, which yielded the best results, *i.e.* the most accurate rotational parameters for the subsequent translation search (Table 2). The top 30 rotational peaks were used to calculate the translation function. The translation function seemed more susceptible to the data resolution cut-off than the rotation function. Distinguishable solutions were found in the translation function computed with 12–3.5 Å resolution data only for the cross-rotation peaks 1 and 4 (Table 2). The most prominent solution (peak 1) was fixed in order to search for other solutions. Six promising translation solutions were picked out according to the *R* factor, correlation coefficient and the value of the translation function compared with the noise. A round of rigid-body fitting using 12–3.0 Å data resulted in an *R* factor of 0.393 and a correlation coefficient of 0.644. The six molecules (named *L*1, *L*2, *M*1, *M*2, *N*1 and *N*2 in Table 2) in the unit cell were then checked and no severe overlap was observed. *N*1 and *N*2 are obviously *A*-centring symmetry-related solutions, and *L*1 and *L*2, *M*1 and *M*2 also reveal *A*-centring symmetry relationships after application of the proper crystallographic symmetrical operations (Table 2). This is consistent with the analysis of diffraction data and Patterson function.

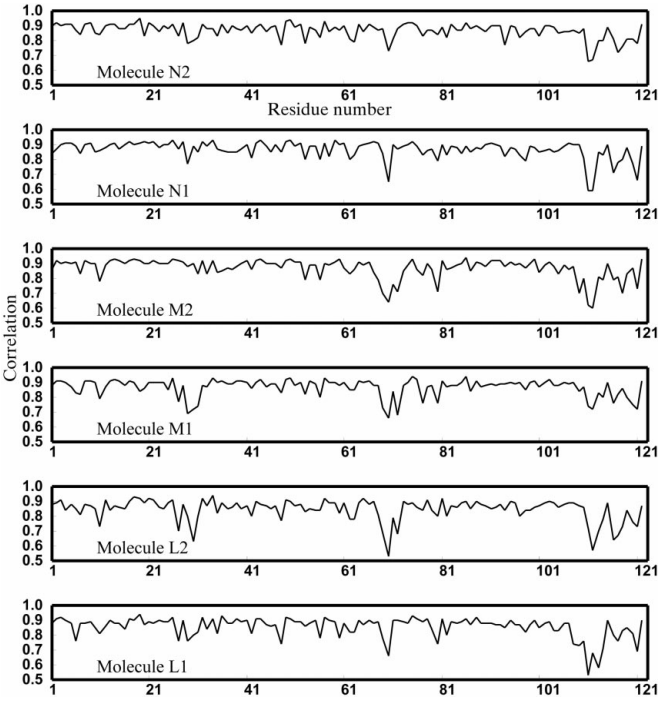

Figure 2
Real-space correlation coefficient per residue between the final model and the 2*Fo* − *Fc* electron-density map, calculated with the program *O* (Jones *et al.*, 1991) with parameters A_o = 0.9, *C* = 0.75. Residues are numbered continuously.

Table 2
Molecular replacement.

Corr, correlation coefficient; α, β, γ, Eulerian angles; *x*, *y*, *z*, fractional Cartesian coordinates. Values in parentheses are the highest noise peaks.

Cross-rotation function.

Peak number	α	β	γ	Corr
1	157.20	79.55	39.38	14.7 (14.0)
3	173.73	85.80	283.33	12.8
4	20.02	81.70	345.56	12.6
5	5.93	90.00	103.55	11.5
20	28.37	90.00	226.14	9.2

Translation function.

Peak number	*x*	*y*	*z*	Corr	*R*
1	0.14628	0.35369	0.02391	14.2 (11.3)	55.0 (55.8)
4	0.10010	0.45781	0.18839	15.7 (13.4)	54.5 (55.2)

Fixed	Search	*x*	*y*	*z*	Corr	*R*
1	3	0.35403	0.39271	0.28124	20.1 (16.3)	53.2 (54.3)
1	4*a*†	0.60845	0.97994	0.67198	21.9 (18.2)	52.9 (54.1)
1	4*b*†	0.60219	0.45668	0.18754	21.3 (18.2)	53.1 (54.1)
1	5	0.64470	0.89336	0.21905	18.1 (14.6)	53.7 (55.0)
1	20	0.85158	0.35299	0.98163	17.3 (13.1)	54.9 (56.4)

Rigid-body fitting.

α	β	γ	*x*	*y*	*z*	Corr	*R*	Monomer
156.90	78.54	37.44	0.15017	0.35480	0.02433	64.4	39.3	*L*1
170.91	76.44	281.10	0.36438	0.92166	0.77932	64.4	39.3	*M*1
17.06	82.25	346.77	0.60967	0.98376	0.67127	64.4	39.3	*N*1
19.99	79.63	344.12	0.60350	0.45678	0.18837	64.4	39.3	*N*2
6.70	93.90	104.62	0.64579	0.89211	0.21844	64.4	39.3	*M*2
25.30	95.56	223.34	0.86236	0.35479	0.98222	64.4	39.3	*L*2

† The cross-rotation peak 4 has two translation solutions, 4*a* and 4*b*, which are related by pseudo-*A*-centring symmetry and are referred to as monomers *N*1 and *N*2, respectively. The crystallographic equivalent solutions of monomers *L*1 and *M*1 can be obtained by application of the following proper symmetry operations. *L*1′: α = 23.10, β = 101.46, γ = 217.44°, *x* = 0.84983, *y* = 0.85480, *z* = 0.47567; *M*1′: α = 9.09, β = 103.56, γ = 101.10°, *x* = 0.63562, *y* = 0.42166, *z* = 0.72068. These solutions are obviously related by *A*-centring symmetry to *L*2 and *M*2, respectively.

2.3. Model building and refinement

The program *X-PLOR* (Brünger, 1992*a*) and the stereochemical parameters of Engh & Huber (1991) were used for the crystallographic structure refinement. The positional refinement, restrained individual *B*-factor refinement and the simulated-annealing protocols were performed. The model was refitted using the programs *FRODO* (Jones, 1978) and *O* (Jones *et al.*, 1991) based on the $2F_o - F_c$ and $F_o - F_c$ electron-density maps. During the refinement, the non-crystallographic symmetry restraints [the positional weight constant and σ for the *B* factor are 20 kcal mol^{-1} Å^{-2} and 2 Å^2, respectively, for main-chain atoms and 5 kcal mol^{-1} Å^{-2} and 6 Å^2, respectively, for side-chain atoms (1 kcal mol^{-1} Å^{-2} = 4.184 kJ mol^{-1} Å^{-2})] were applied to each single molecule except for residues 30–32, which show variable local confor-

mations (see below). 10% of data in a number of randomly selected thin resolution spheres (*DATAMAN* program; Kleywegt & Jones, 1996) were excluded before any refinement for the calculation of the free *R* factor (Brünger, 1992*b*) in order to monitor the whole refinement procedure.

The six molecular-replacement solutions were first subjected to a round of rigid-body refinement defining each molecule as a group; *R* and $R_{\rm free}$ were reduced to 0.422 and 0.430, respectively, at 3.0 Å resolution. Data in the 8–2.8 Å resolution range with $F > 2\sigma$ were then included. After cycles of refinement and model building, the *R* factor dropped to 0.214 with an $R_{\rm free}$ of 0.282. Significant additional peaks were found in the electron-density maps and were assigned to Ca^{2+} ions. Bulk-solvent correction was then applied for all data (30–2.8 Å, $F > 2\sigma$), which resulted in an *R* and $R_{\rm free}$ of 0.221 and 0.268, respectively. For data at 30–5.6 Å resolution, *R* and $R_{\rm free}$ dropped from 0.471 and 0.481 to 0.271 and 0.281, respectively. Water molecules were added based on the $2F_o - F_c$ and $F_o - F_c$ electron-density maps and were checked for formation of hydrogen bonds. The current model contains 5826 non-H atoms, including three intermolecular Ca^{2+} ions, five intramolecular Ca^{2+} ions and 17 water molecules (Table 1). The crystallographic *R* factor is 0.194 (30–2.8 Å, $F > 2\sigma$, 23582 reflections) and the $R_{\rm free}$ value is 0.260. The overall real-space correlation coefficient between the final model and the $2F_o - F_c$ electron-density map is 0.87 (Fig. 2, calculated with the program *O*; Jones *et al.*, 1991). R.m.s.d.s from ideal values for bond lengths and bond angles are 0.007 Å and 1.1°, respectively. The mean coordinate error of all atoms estimated using Luzzati plots (Luzzati, 1952) is 0.30 Å. The stereochemistry was checked using the program *PROCHECK* (Laskowski *et al.*, 1993). The overall *G* factor is 0.22. All the non-glycine residues lie in the allowed regions and 88.5% of the residues are in the most favoured regions of the Ramachandran plot (Ramachandran & Sasisekharan, 1968; Fig. 3). The *B*-factor distributions for main-chain and side-chain atoms are shown in Fig. 4.

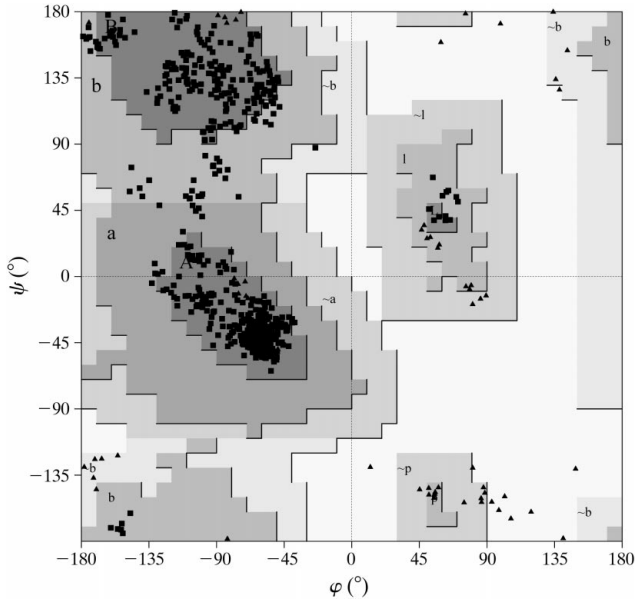

Figure 3
Ramachandran plot. 88.5% of residues are in the most favoured regions (A, B, L); 11.3% are in the additional allowed regions (a, b, l, p); 0.2% are in the generously allowed regions (~a, ~b, ~l, ~p); glycine residues are shown as triangles.

3. Results and discussion

3.1. Structure

The structure of ATX crystallized at pH 8.5 has been determined at 2.8 Å resolution by the molecular-replacement method and refined to a crystallographic *R* factor of 0.194 with excellent stereochemistry. The final $2F_o - F_c$ electron-density map shows good agreement with the atomic model. Crystal packing reveals obvious pseudo-*A*-centring symmetry (Fig. 5*a*). The asymmetric unit contains six molecules named *L*1, *L*2, *M*1, *M*2, *N*1 and *N*2 (Fig. 5*b*) as in the molecular replacement. The pseudo-*A*-centring symmetry in $P2_12_12_1$ is equivalent to a non-crystallographic twofold axis which lies parallel to the crystallographic *b* or *c* axis. Thus, the six molecules can be divided into two groups related by the twofold NCS: *N*1, *M*2 and *L*1, and *N*2, *M*1 and *L*2. The relationship between the six molecules shows significant deviations from exact *A*-centring symmetry, which could arise partially from non-specificity of the hydrophobic intermolecular interactions (see §3.3). All the molecules lie in an orientation with the planes defined by two long helices (residues 39–55 and 89–110) approximately parallel to the *bc* plane of the unit cell. The molecular packing is completely different from that seen at pH 4.5 as a 'dimer-of-dimers'-like structure

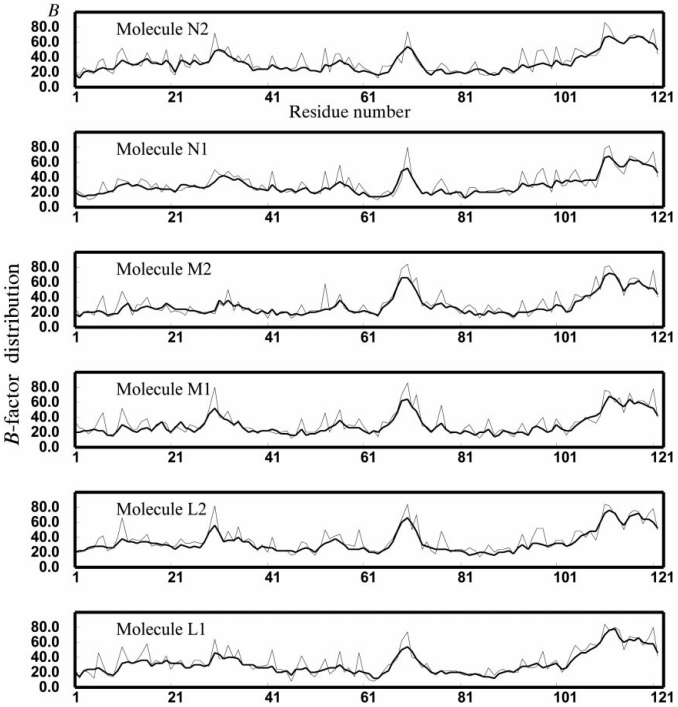

Figure 4
The *B*-factor distribution per residue. Thick line, main chain; thin line, side chain. Residues are numbered continuously.

(Tang *et al.*, 1998). In fact, the molecular arrangement in the pH 4.5 structure could not be maintained under basic conditions owing to the intradimeric close contacts of 2.45 Å between the side-chain atoms Glu93 OE1 and Glu97 OE1, which could only be protonated at pH 4.5. Moreover, the molecular packing is also different from that of human non-pancreatic secreted PLA_2 complexed with an analogue of a phospholipid, which also has six molecules per asymmetric unit (Oh, 1995). The details of molecular packing will be described and discussed below.

The overall folding of ATX in the orthorhombic form is that of a typical group II secretory PLA_2. The two long antiparallel α-helices (residues 39–55 and 89–110) define a platform on which the N-terminal helix (residues 1–15), the Ca^{2+}-binding loop (residues 25–35), the so-called β-wing (residues 74–85) and the C-terminal ridge cross-linked by seven disulfide bonds are situated.

Pairwise C^{α} superposition between molecules *N*1, *N*2, *M*1, *L*1 and *L*2 results in r.m.s.d.s of ∼0.20 Å, while the r.m.s.d. between molecule *M*2 and the other five molecules ranges from 0.31 Å (molecules *M*2 and *M*1) to 0.38 Å (molecules *M*2 and *N*2) owing to the distinct structure of the Ca^{2+}-binding loop in molecule *M*2. Ca^{2+} ions were found in the Ca^{2+}-binding loops of molecules *N*1, *N*2, *M*1, *L*1 and *L*2, and coordinated with the peptidyl O atoms of residues Tyr28, Gly30, Gly32 and the carboxylate O atoms of Asp49, with the exception of molecule *N*1, which contains the two coordinating water molecules usually found in high-resolution PLA_2 structures. However, the position corresponding to the Ca^{2+} in molecule *M*2 is not occupied by a Ca^{2+}, but by the N^{ξ} atom of residue Lys86 of molecule *L*1, which forms a salt bridge with the carboxylate group of Asp49 with a distance of 2.72 Å (Fig. 6).

The monomeric structure of ATX at pH 8.5 reported here is virtually superposable with that in the $P2_1$ space group crystallized at pH 4.5 (PDB entry code: 1a2a); the resultant r.m.s.d. is 0.70 Å for all C^{α} atoms of molecule *A* in the $P2_1$ structure and molecule *N*2 in the present structure. The structure of the catalytic network consisting of His48, Asp99, Tyr52 and Tyr73 is highly conserved and is not affected by the variation in the pH of the crystallization conditions. These data indicate less flexibility in the remainder of ATX structure. The only significant difference occurs at the tip of the β-wings (Fig. 7). Residues 78–81 twist away from the molecular core and the maximum deviation between equivalent C^{α} atoms of these residues is 3.41 Å (for residue 79). The rotomer conformation of the aromatic ring of residue Tyr81 changes by about 120° around the $C^{\alpha}-C^{\beta}$ bond. These differences may be a consequence of the different environments of these residues. For example, the ξ-amino group of Lys78 in molecule *N*2 forms a salt bridge with the carboxylate group of Asp111 from molecule *M*2. The phenyl plane of Tyr81 from molecule *N*2 is nearly parallel to the guanidine plane of Arg108 from molecule *M*2, with a centroid distance of ∼3.7 Å. In the pH 4.5 structure, the β-wing tips participate in the intradimeric interactions (hydrogen bonds involving residues 77, 78, 80, 81, 82 and aromatic–aromatic interactions between side chains of residues Tyr81) and interdimeric interactions (hydrogen bonds between peptidyl N and O atoms of residues Ile77). The local conformation of the proposed neurotoxic site (Tang *et al.*, 1998), *i.e.* turn 55–61 and stretch 85–91, is virtually the same as that of the $P2_1$ structure (r.m.s.d. is 0.35 Å for C^{α} and 0.63 Å for all atoms excluding the surface side-chain atoms of residues Asn59 and Lys86). The conformational stability of the neurotoxic site might be advantageous for ATX to readily fit the specific acceptor on the presynaptic membrane.

The sequence of ATX used for crystallization was not determined. Residue 31 in the crystal structure of ATX at pH 4.5 was assigned as a Gly according to the sequence reported previously (Kondo *et al.*, 1989) and the region of residues 30–33 is poorly defined in the $2F_o - F_c$ electron-

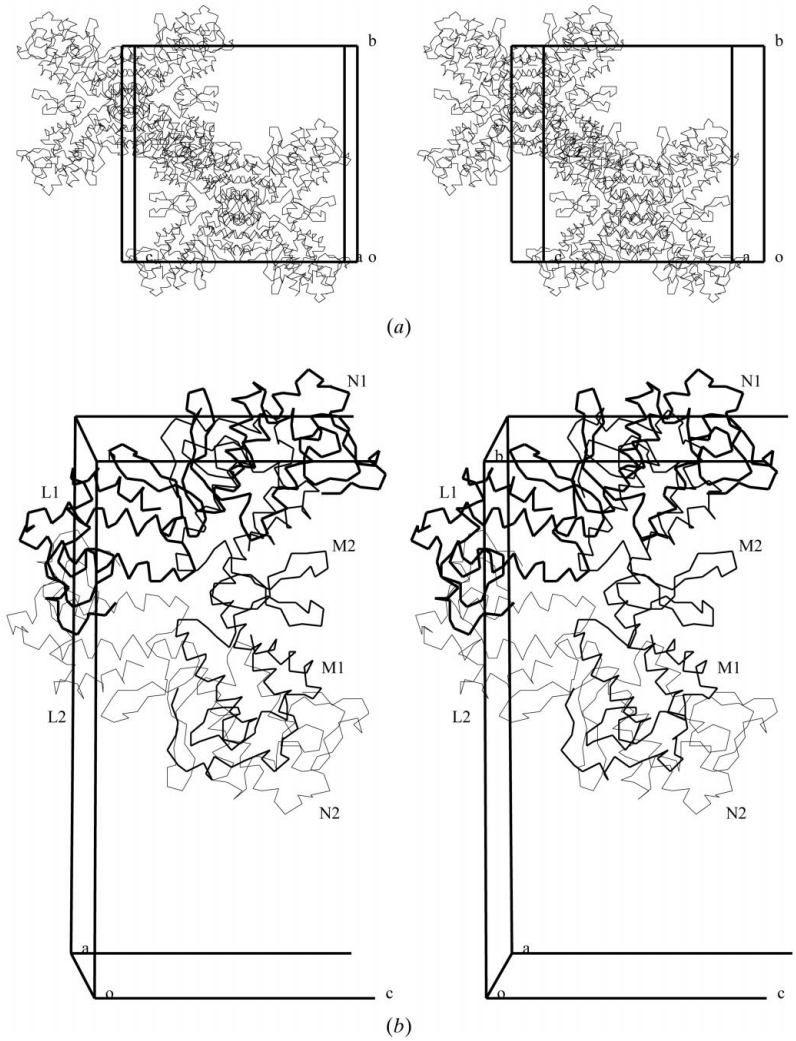

Figure 5
(*a*) Crystal packing showing the pseudo-*A*-centring symmetry. (*b*) Six molecules in the asymmetric unit. Both are viewed down the crystallographic *a* axis.

density map (Tang *et al.*, 1998). However, in the present electron-density map, residue 31 is clearly a Trp, even though the starting model taken from the structure of ATX at pH 4.5 has a Gly at position 31. During refinement, significant peaks above the 2σ level appeared near the C^{α} atoms of residues 31 in the $2F_o - F_c$ electron-density map and could be properly allocated to Trp side chains (Fig. 6). For this reason, Trps were assigned to position 31 of all six molecules of this ATX isoform. The side chain of Trp31 from molecule *M*2 has the best defined electron density, with a mean *B* value of 19.1 Å^2, while the corresponding electron density in molecule *L*2 is the weakest of all the molecules. Fluorescence spectroscopy revealed that there may be Trp in ATX (Zheng *et al.*, 1993). It is also possible that ATX may exist as isoforms which contain Trp or Gly at position 31. The presence of isoforms is frequently observed for PLA_2 presynaptic neurotoxins, *e.g.* crotoxin (Faure & Bon, 1989) and ammodytoxin (Ritonja & Gubensek, 1985).

3.2. Intermolecular Ca^{2+} ions

Besides the ordinary intramolecular Ca^{2+} ions in the Ca^{2+}-binding loops, three intermolecular Ca^{2+} ions have been found between molecules *N*2 and *L*2, *M*2 and *M*1, and *L*1 and *N*1. Thus, the six molecules in the asymmetric unit can be divided into three similar Ca^{2+}-linked dimers, *N*2–*L*2, *M*2–*M*1 and *L*1–*N*1 (Fig. 8*a*). The non-crystallographic symmetry operations mapping *N*2–*L*2 to *M*2–*M*1 and *M*2–*M*1 to *L*1–*N*1 are a rotation of 120.1° plus a translation of 16.2 Å and a rotation of 113.9° plus a translation of 16.7 Å, respectively. No non-crystallographic threefold screw axis exists because the positions of these rotation axes differ remarkably, although their directions deviate by no more than 3°.

Each intermolecular Ca^{2+} ion is located on the local twofold axis within the dimer and is well coordinated by six O atoms: Asp71 OD1, Glu92 OE2 and Ile72 O from both monomers (Fig. 8*b*). These ligands form a near-perfect octahedron and the average distance from Ca^{2+} (2.46 Å) is close to that revealed in high-resolution crystal structures (2.4 Å; Table 3). This six-ligand octahedral coordinating system is distinct from the usual helix–loop–helix or EF-hand motif of Ca^{2+}-binding proteins, in which the Ca^{2+} ion is located in a pentagonal bipyramid formed by seven chelators (Strynadka & James, 1989).

Table 3
Distances between the intermolecular Ca^{2+} ions and ligands.

Ligand	Distance (Å)	Ca^{2+}
*N*2 Asp71 OD1	2.38	CA1
*N*2 Ile72 O	2.44	
*N*2 Glu92 OE2	2.53	
*L*2 Asp71 OD1	2.39	
*L*2 Ile72 O	2.45	
*L*2 Glu92 OE2	2.57	
*M*2 Asp71 OD1	2.44	CA2
*M*2 Ile72 O	2.45	
*M*2 Glu92 OE2	2.44	
*M*1 Asp71 OD1	2.60	
*M*1 Ile72 O	2.54	
*M*1 Glu92 OE2	2.35	
*N*1 Asp71 OD1	2.53	CA3
*N*1 Ile72 O	2.44	
*N*1 Glu92 OE2	2.34	
*L*1 Asp71 OD1	2.45	
*L*1 Ile72 O	2.38	
*L*1 Glu92 OE2	2.49	

The structure of porcine pancreatic PLA_2 (Thunnissen *et al.*, 1990; PDB entry code 2phi) revealed a Ca^{2+}-linked dimer; the Ca^{2+} also lies in the centre of an octahedron formed by O-atom ligands from corresponding residues. However, the arrangement of the six coordinating atoms differs interestingly from our structure (Fig. 8*c*). When three coordinating atoms from one monomer (*e.g. N*2 of ATX) are properly superposed onto the corresponding atoms from one monomer of 2phi, the other three coordinating atoms from residues 71, 72 and 92 of monomer *L*2 take the positions of 72, 92 and 71 from monomer *B* of 2phi, respectively. Although the Ca^{2+} ion is the sole connection between two monomers in both cases, the Ca^{2+}-linked dimer of 2phi cannot be arranged as it is in ATX. One reason is the difference in the side-chain length of residue 71, which provides a pair of ligands for Ca^{2+}. Residue 71 of ATX is Asp, while in 2phi it is Glu. This one bond-length difference will cause an extreme deviation of the dimeric arrangement because it occurs near the local twofold axis between monomers. Another reason, which might be more important, lies in the 'pancreatic loop' (residues 62–66 in 2phi; Arni & Ward, 1996), which does not exist in ATX and is one of the criteria for differentiation of group II PLA_2s from group I (Heinrikson, 1991). If the two monomers of 2phi are

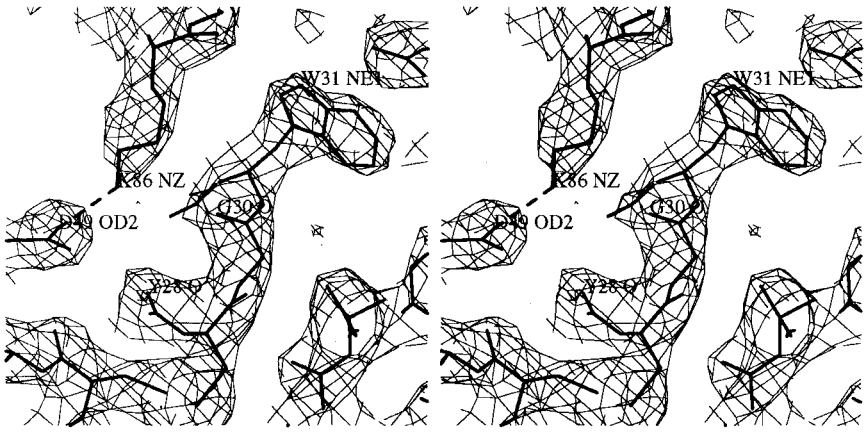

Figure 6
The salt bridge (dashed line) between the ξ-amino group of Lys86 from molecule *L*1 (bold line) and the carboxylate group of Asp49 from molecule *M*2 (solid line). Also shown is the $2F_o - F_c$ electron-density map contoured at 1.3σ calculated during the refinement before the side chain of Trp31 was added to the model.

assumed to be arranged in the same manner as ATX, their 'pancreatic loops' would overlap severely (Fig. 8*b*).

The three intermolecular Ca^{2+} ions have a mean *B* value of 16.1 Å^2 in the final model and their electron densities in the $2F_o - F_c$ map are above the 6σ level, while the mean *B* value of the intramolecular Ca^{2+} ions is 41.8 Å^2. Since both types of Ca^{2+} binding occur under the same crystallization conditions, it seems that Ca^{2+} binding is preferential for the intermolecular sites compared with the intramolecular sites, *i.e.* the intermolecular sites might have a higher association constant for Ca^{2+} binding. This may be because of the extensive electrostatic interactions between Ca^{2+} ions and the four carboxylate ligands, the basic pH and the proper stereochemistry of the involved ligands. Notably, the carboxylate ligands Glu92 and Asp71 lie within or near the putative neurotoxic site, *i.e.* two adjacent regions around turn 55–61 and stretch 85–91, and the negative charge of Glu92 is unique for presynaptically neurotoxic PLA_2s (Tang *et al.*, 1998). Presumably, the strong tendency of these acidic residues to bind positively charged ions might be significant for ATX–acceptor recognition. Similar intermolecular Ca^{2+} ions play an important role in the assembly and disassembly of many viruses (Durham, 1978; Ilag *et al.*, 1994). Such Ca^{2+}-binding sites can be incorporated into the target protein in order to provide strong directional interactions for protein–protein association and protein stabilization, which may be useful in protein engineering and design.

3.3. Intermolecular hydrophobic interactions

Extensive intermolecular hydrophobic interactions occur at three hydrophobic molecular interfaces between molecules *N*2 and *M*1, molecules *N*1 and *M*2, and molecules *L*2 and *L*1 (Figs. 9*a*, 9*b*, 9*c* and 9*e*). The molecular assemblage within each of the three molecular pairs is in a face-to-face manner, *i.e.* the entrances to the hydrophobic channels surrounded by residues Leu2, Leu3, Asn6, Ile19, Phe21, Trp31 and Lys69, through which the catalytically active residue His48 is accessible to substrates, are shielded in the interior interface. The details of the three interfaces are quite different. The relative molecular position and orientation within each molecular pair are to some extent variable owing to the non-specific nature of the hydrophobic interactions therein. The non-crystallographic operation which maps *N*2 to *M*1 is a rotation of 171.1° plus a translation of 4.71 Å along the rotation axis; the corresponding parameters for *N*1 and *M*2 are 178.0° and 8.66 Å, respectively. The relative orientation of two molecules within molecular pairs *N*2–*M*1 and *N*1–*M*2 deviates by 9.4°, while the relative position along the local twofold axis within pair *N*1–*M*2 is 3.95 Å larger than pair *N*2–*M*1. The non-crystallographic operation which maps *L*2 to *L*1 is a rotation of 179.0° plus a translation of 1.24 Å along the rotation axis and the relative orientation between the two molecules is nearly the opposite of that between *N*2–*M*1 and *N*1–*M*2. The losses of solvent-accessible surface area caused by the hydrophobic contacts for dimers *N*2–*M*1, *N*1–*M*2 and *L*2–*L*1 are 433.5, 539.4 and 769.5 Å^2, respectively (the solvent-accessible surface area of one molecule is ~5700 Å^2). Among the three pairs, *N*2–*M*1 and *N*1–*M*2 are generally similar to each other, as they are related by the twofold NCS.

Table 4
Side-chain atoms involved in the intermolecular hydrophobic interactions (distance < 4.0 Å).

Atom 1	Atom 2
*N*2 Leu2 CD2	*M*1 Trp31 CH2
*N*2 Leu3 CD2	*M*1 Trp31 CB
*N*2 Ile19 CG2	*M*1 Phe119 CD2
*N*2 Ile19 CD	*M*1 Phe24 CE1
*N*2 Phe24 CE1	*M*1 Pro20 CB
*N*2 Phe24 CZ	*M*1 Phe119 CZ
*N*2 Trp31 CE2	*M*1 Ile19 CD
*N*1 Leu3 CD2	*M*2 Trp31 CB
*N*1 Ala18 CB	*M*2 Phe119 CE2
*N*1 Ile19 CG1	*M*2 Phe119 CE1
*N*1 Ile19 CD	*M*2 Pro20 CB
*N*1 Ile19 CD	*M*2 Met118 CG
*N*1 Ile19 CD	*M*2 Phe119 CE1
*N*1 Phe24 CZ	*M*2 Pro20 CG
*N*1 Trp31 CZ3	*M*2 Ile19 CD
*L*2 Leu2 CD1	*L*1 Phe119 CE2
*L*2 Ile19 CD	*L*1 Ile19 CD
*L*2 Phe24 CD1	*L*1 Trp31 CB
*L*2 Trp31 CZ2	*L*1 Tyr120 CA
*L*2 Trp31 CH2	*L*1 Phe119 CB
*L*2 Phe119 CB	*L*1 Trp31 CZ2

The hydrophobic residues participating in the interfacial interactions, including Leu2, Leu3, Ala18, Ile19, Pro20, Phe24, Trp31, Met118 and Phe119 (Table 4), lie at the so-called interfacial recognition site and form a relatively flat extended hydrophobic area (Dijkstra *et al.*, 1981; Heinrikson & Kezdy, 1990; Biltonen *et al.*, 1990). The entrances to the hydrophobic channels of molecules *N*2 and *N*1 are completely occluded by side chains of residues Phe24 and Trp31 from molecule *M*1 and residues Pro20 and Phe24 from molecule

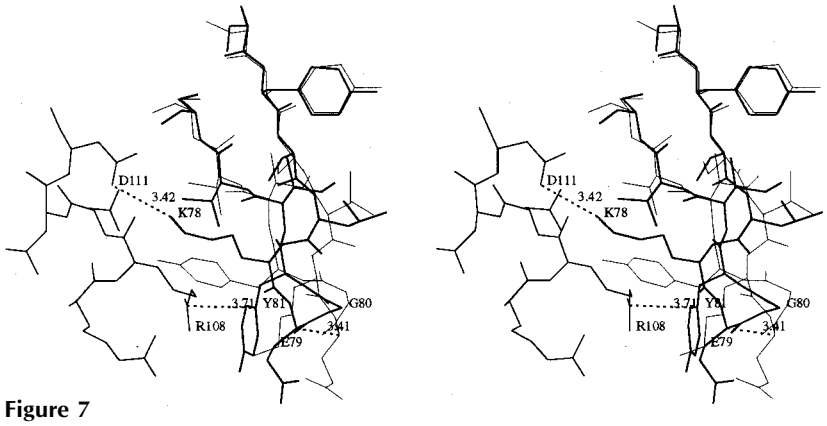

Figure 7
The β-wing tip. Bold line, molecule *N*2; solid line, molecule *M*2; thin line, molecule *A* of the $P2_12_12_1$ structure superposed onto the $P2_12_12_1$ structure. Dashed line, distances between atoms (Å).

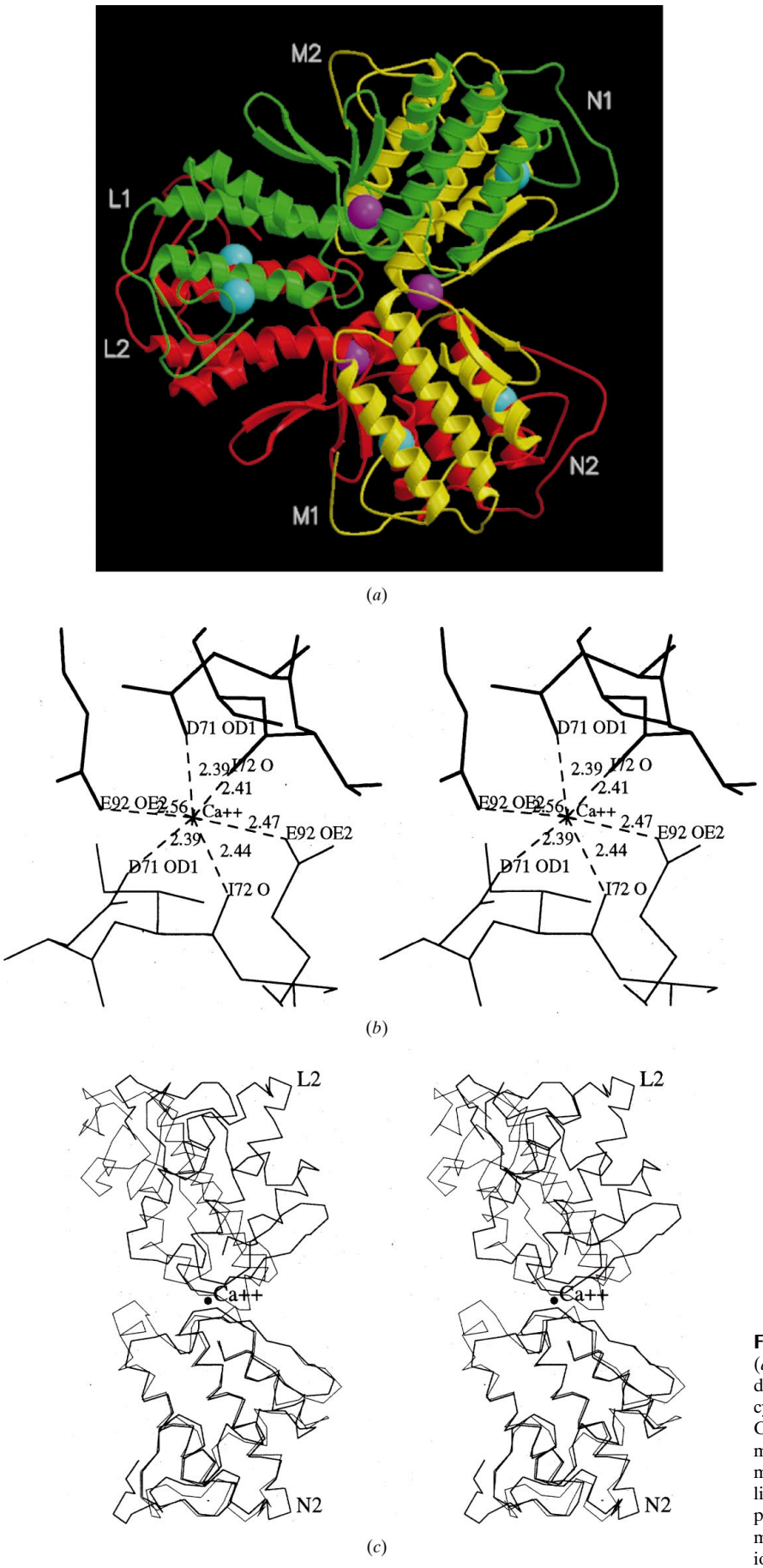

*M*2, respectively, while those of molecules *M*2, *M*1, *L*2 and *L*1 are only partially covered. In particular, the side chain of Trp31 from molecule *L*2 fits well into a small surface depression of molecule *L*1 surrounded by residues 24–31 and 119–122, and the indole ring is nearly parallel with the phenyl rings of Phe24 and Phe119 from molecule *L*1 (Fig. 9*d*). Similarly, the side chain of Trp31 from molecule *L*1 also inserts into the corresponding region of molecule *L*2. These hydrophobic interactions might mimic those occurring at the PLA_2–membrane interface. Each member of the molecular pair serves as the phospholipid bilayer surface for its partner. The protein molecule contacts the membrane *via* its flat interfacial recognition site and, meanwhile, the indole ring of Trp31 may insert into the phospholipid region as a membrane anchor to stabilize the PLA_2–membrane complex, which may contribute to the interfacial activation of PLA_2 on the membrane.

In the structure of ATX crystallized at pH4.5, two sets of residues Ile19, Pro20, Ala23, Phe24, Met118 and Phe119 from a pair of adjacent molecules form a hydrophobic interface and their interactions play a central role in the crystal packing (Tang *et al.*, 1998). This implies that the intermolecular hydrophobic interactions along the interfacial recognition site are strong, although non-specific, and seem independent of solvent conditions. It is possible that, driven by hydrophobic effects, the molecular pairs in the present structure could also form in solution, which might explain the tendency of ATX towards aggregation. This hydrophobic interaction-induced molecular association suggests a self-protection mechanism for ATX. In solution, ATX molecules could be associated into hydrophobic interaction-

Figure 8
(*a*) Ribbon diagram representation of the Ca^{2+}-linked dimers. Red, *N*2–*L*2; green, *L*1–*N*1; yellow, *M*2–*M*1; cyan, intramolecular Ca^{2+} ions; purple, intermolecular Ca^{2+} ions. (*b*) The coordinating system of the intermolecular Ca^{2+} ion. Bold line, molecule *N*2; thin line, molecule *L*2. Dashed line, distances between Ca^{2+} and ligands. (*c*) The Ca^{2+}-linked dimer (bold line). The porcine pancreatic PLA_2 (thin line) is superposed onto molecule *N*2. Small spheres are the intermolecular Ca^{2+} ions.

related molecular pairs. Hence, the interfacial recognition sites and the entrances to the hydrophobic channel of both ATX molecules are masked from the solvent by its partner, which prevents the neurotoxin from promiscuously binding to non-targeting membrane and avoids exhaustion of neurotoxin molecules en route to the presynaptic membrane. Structural analysis showed that the entrance to the hydrophobic channel of the PLA_2 subunit of vipoxin, a heterodimeric presynaptic neurotoxin, is masked by its inhibitory subunit (Perbandt *et al.*, 1997). Thus, the self-protection mechanism proposed here is to some extent similar to that of vipoxin. In other words, ATX might act as a homodimeric neurotoxin. It is widely accepted that PLA_2 presynaptic neurotoxins might interact with specific acceptors on the presynaptic membranes *via* the neurotoxic sites at the molecular surface (Tzeng, 1993; Kwong *et al.*, 1995) and several groups have reported the purification and characterization of membrane proteins which might serve as the acceptors for presynaptic neurotoxins (Hseu *et al.*, 1990; Yen & Tzeng, 1991). It has been proposed that the regions around turn 55–61 and stretch 85–91, which show unique local conformation and electrostatic characteristics, might be the neurotoxic site of ATX, *i.e.* the site responsible for neurotoxin–acceptor recognition (Tang *et al.*, 1998). PLA_2 activity is essential for ATX to exert presynaptic neurotoxicity. Covalent modification of the catalytically active residue His48 of ATX by *p*-bromophenacyl bromide results in simultaneous loss of PLA_2 and neurotoxic activities (Kondo *et al.*, 1989), as reported for other presynaptic neurotoxins (Yang, 1994; Hawgood & Bon, 1991).

Considering these data, a neurotoxic mechanism for ATX emerges as the following: (i) the neurotoxin molecules diffuse towards the presynaptic membrane as molecular pairs held together by hydrophobic interactions between the interfacial recognition sites and (ii) upon reaching the presynaptic membrane, the neurotoxin

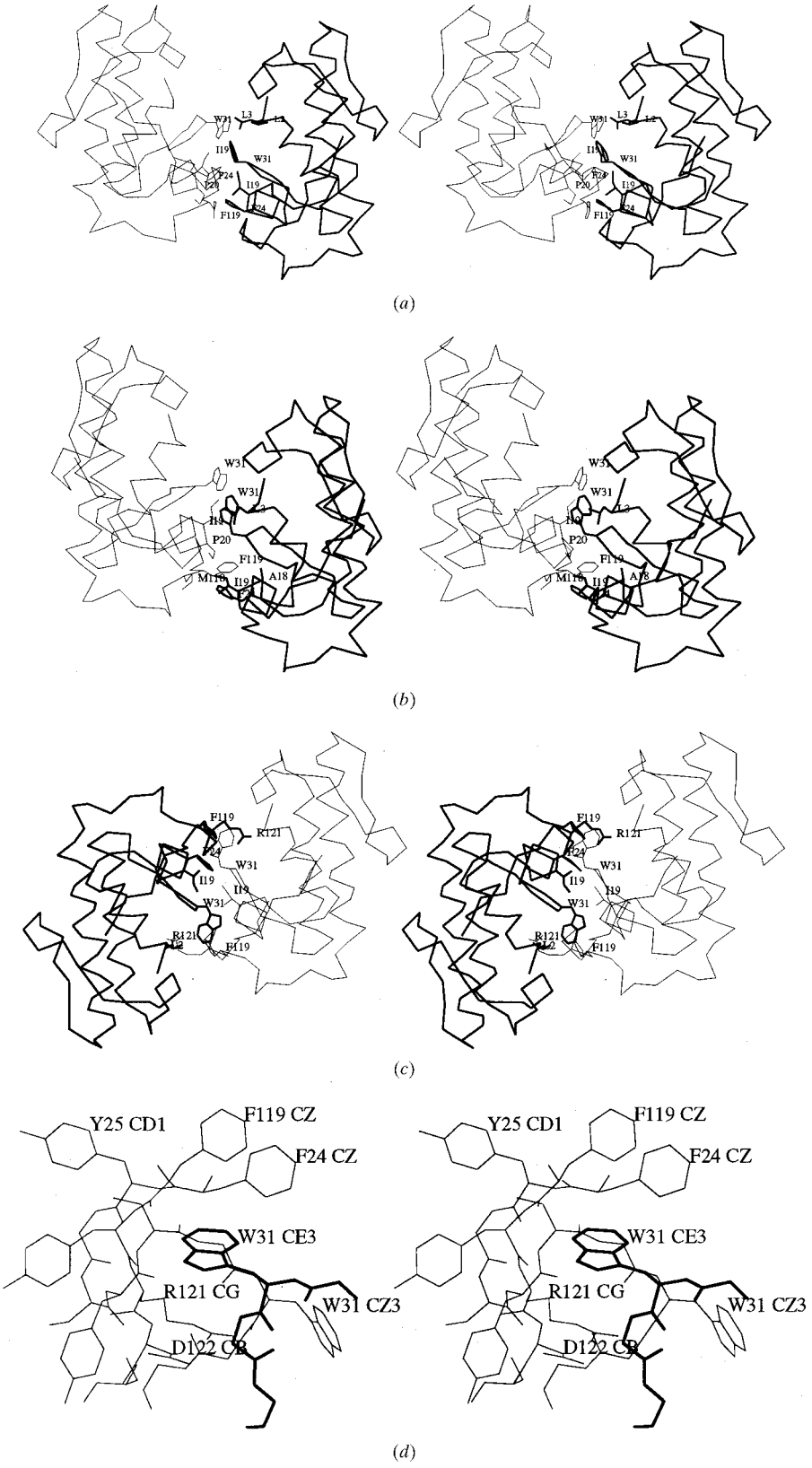

Figure 9
Molecular pairs *N*2–*M*1 (*a*), *N*1–*M*2 (*b*) and *L*2–*L*1 (*c*) induced by the hydrophobic interactions along the interfacial recognition sites and (*d*) the local structure around Trp31 of molecule *L*2. Bold line, molecules *N*2, *N*1 and *L*2; thin line, *M*2, *M*1 and *L*1.

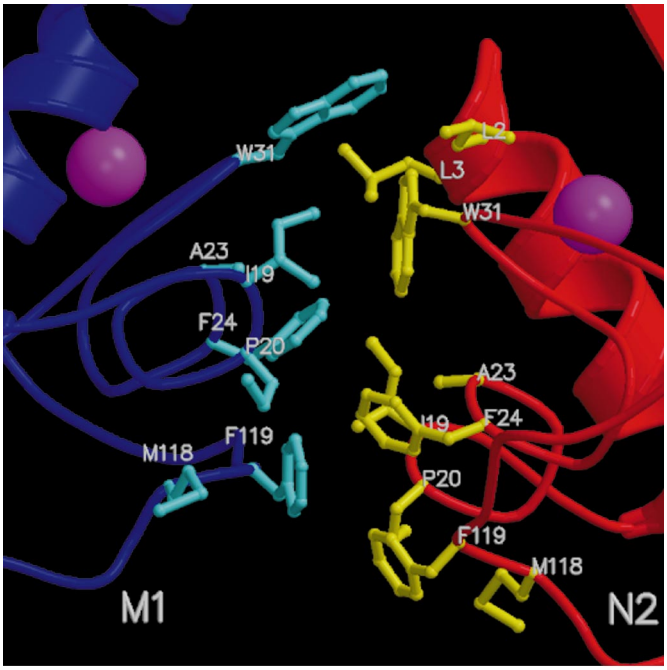

(*e*)

Figure 9 (continued)
(*e*) The hydrophobic interactions in *N*2–*M*1. Red, *N*2; blue, *M*1; yellow, side chains of *N*2; cyan, side chains of *M*1; purple, intramolecular Ca^{2+} ions.

molecule recognizes and binds the specific acceptor *via* its neurotoxic site. The self-association of neurotoxin molecules breaks down. The interfacial recognition site is exposed to the membrane such that the neurotoxin molecule can exert its PLA_2 activity to destroy the presynaptic membrane and finally block the neurotransmission (Fig. 10).

We thank SERC Daresbury Laboratory for providing the *CCP*4 program suite and T. A. Jones and G. J. Kleywegt for providing the programs *O* and *DATAMAN*. This project was supported by the Academia Sinica.

References

Arni, R. K. & Ward, R. J. (1996). *Toxicon*, **34**(8), 827–841.
Biltonen, R. L., Heimburg, T. R., Lathrop, B. K. & Bell, J. D. (1990). *Adv. Exp. Med. Biol.* **279**, 85–103.
Bon, C., Changeux, J.-P., Jeng, P. W. & Fraenkel-Conrat, H. (1979). *Eur. J. Biochem.* **99**, 471–481.
Brünger, A. T. (1992*a*). *X-PLOR Manual, Version* 3.1. Yale University, New Haven, Connecticut, USA.
Brünger, A. T. (1992*b*). *Nature (London)*, **355**, 472–475.
Chen, Y.-C., Maraganore, J. M., Reardon, I. & Heinrikson, R. L. (1987). *Toxicon*, **25**(4), 401–409.
Chen, Y.-C., Wu, X.-F., Zhang, J.-K., Jiang, M.-S. & Hsu, K. (1981). *Acta Biochim. Biophys. Sin.* **13**, 205–212.
Collaborative Computional Project, Number 4 (1994). *Acta Cryst.* D**50**, 760–763.
Dennis, E. (1994). *J. Biol. Chem.* **269**(18), 13057–13060.
Dijkstra, B. W., Drenth, J. & Kalk, K. H. (1981). *Nature (London)*, **289**, 604–606.
Durham, A. C. H. (1978). *Hoppe-Seyler's Z. Physiol. Chem.* **359**, 1047–1051.
Engh, R. A. & Huber, R. (1991). *Acta Cryst.* A**47**, 392–400.
Faure, G. & Bon, C. (1989). *Biochemistry*, **27**, 730–738.
Hawgood, B. J. & Bon, C. (1991). *Handbook of Natural Toxins. Reptile Venoms and Toxins*, Vol. 7, edited by A. T. Tu, pp. 3–52. New York: Marcel Dekker.
Heinrikson, R. L. (1991). *Methods Enzymol.* **197**, 201–215.
Heinrikson, R. L. & Kezdy, F. J. (1990). *Adv. Exp. Med. Biol.* **279**, 37–47.
Hseu, M. J., Guillory, R. J. & Tzeng, M. C. (1990). *J. Bioenerg. Biomembr.* **22** (1), 39–50.
Ilag, L. L., McKenna, R., Yadav, M. P., BeMiller, J. N., Incardona, N. L. & Rossmann, M. G. (1994). *J. Mol. Biol.* **244**, 291–300.
Jin, L., Gui, L.-L., Bi, R.-C. & Lin, Z.-J. (1990). *Acta Biochim. Biophys. Sin.* **22**(4), 313–320.
Jones, T. A. (1978). *J. Appl. Cryst.* **11**, 268–272.
Jones, T. A., Zou, J.-Y. & Cowan, S. W. (1991). *Acta Cryst.* A**47**, 110–119.
Kleywegt, G. J. & Jones, T. A. (1996). *Acta Cryst.* D**52**, 826–828.
Kondo, K., Zhang, J.-K., Xu, K. & Kagamiyama, H. (1989). *J. Biochem.* **105**, 1196–203.
Kwong, P. D., McDonald, N. Q., Sigler, P. B. & Hendrickson, W. A. (1995). *Structure*, **3**, 1109–1119.
Laskowski, R., MacArthur, M., Moss, D. & Thornton, J. (1993). *J. Appl. Cryst.* **26**, 283–290.

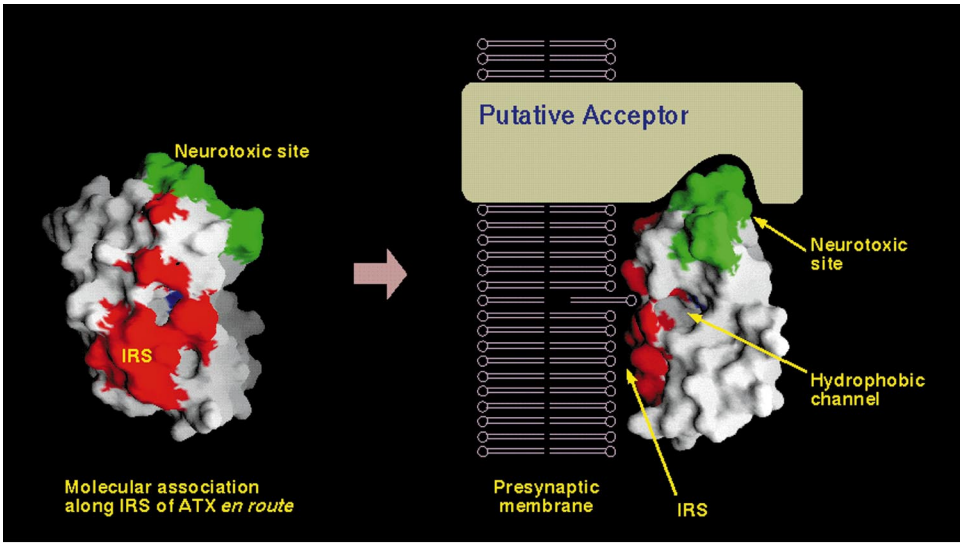

(*a*) (*b*)

Figure 10
Schematic presentation of the neurotoxic mechanism of ATX: (*a*) molecular association along the interfacial recognition site (IRS) during diffusion from the place of injection to the acceptor of the target cell; (*b*) neurotoxin–acceptor recognition and exertion of PLA_2 activity at the presynaptic membrane. The orientation of (*b*) is 90° along the vertical axis from (*a*). Molecular surfaces are generated with the program *GRASP* (Nicholls *et al.*, 1991). Green, neurotoxic site; red, hydrophobic residues at the interfacial recognition site; purple, catalytically active residue His48.

Li, D.-N., Gui, L.-L., Song, S.-Y., Lin, Z.-J., Qian, R. & Zhou, Y.-C. (1995). *Chin. Sci. Bull.* **40**, 664–667.
Luzzati, P. V. (1952). *Acta Cryst.* **5**, 802–810.
Matthews, B. W. (1968). *J. Mol. Biol.* **33**, 491–497.
Mukherjee, A. B., Miele, L. & Pattabiraman, N. (1994). *Biochem. Pharmacol.* **48**(1), 1–10.
Navaza, J. (1994). *Acta Cryst.* A**50**, 157–163.
Nicholls, A., Sharp, K. A. & Honig, B. (1991). *Proteins Struct. Funct. Genet.* **11**, 281–296.
Oh, B.-H. (1995). *Acta Cryst.* D**51**, 140–144.
Perbandt, M., Wilson, J. C., Mancheva, I., Aleksiev, B., Genov, N., Eschenburg, S., Willingmann, P., Weber, W., Singh, T. P. & Betzel, C. H. (1997). *FEBS Lett.* **412**, 573–577.
Ramachandran, G. N. & Sasisekharan, V. (1968). *Adv. Protein Chem.* **23**, 283–291.
Ritonja, A. & Gubensek, F. (1985). *Biochim. Biophys. Acta*, **828**, 306–312.
Rossmann, M. G. & Blow, D. M. (1962). *Acta Cryst.* **15**, 24–31.
Strynadka, N. C. J. & James, M. N. G. (1989). *Annu. Rev. Biochem.* **58**, 951–998.
Tang, L., Lin, Z.-J. & Zhou, Y.-C. (1997). *Sci. China Ser. C*, **40**(5), 481–487.
Tang, L., Zhou, Y.-C. & Lin, Z.-J. (1998). *J. Mol. Biol.* **282**, 1–11.
Thunnissen, M. M. G. M., Kalk, K. H., Drenth, J. & Dijkstra, B. W. (1990). *J. Mol. Biol.* **216**, 425–439.
Tzeng, M. C. (1993). *J. Toxicol. Toxin Rev.* **12**, 1–62.
Yang, C.-C. (1994). *J. Toxicol. Toxin Rev.* **13**(2), 125–177.
Yen, C.-H. & Tzeng, M.-C. (1991). *Biochemistry*, **30**, 11473–11477.
Zhang, J.-K., Jiang, M.-S., Hsu, K., Chen, Y.-C. & Wu, X.-F. (1981). *Acta Biochim. Biophys. Sin.* **13**, 237–243.
Zheng, L., Ruan, K., Lin, N., Qian R. & Zhou, Y. (1993). *Acta Biophys. Sin.* **9**, 347–351.